Chapter 9

In Situ Characterization of Halide Perovskite Synthesis

Maged Abdelsamie[1], Tim Kodalle[2], Mriganka Singh[2], Carolin M. Sutter-Fella[2,] *

[1] *Materials Sciences Division, Lawrence Berkeley National Laboratory, 1 Cyclotron Rd., Berkeley, 94720 California, USA*

[2] *Molecular Foundry Division, Lawrence Berkeley National Laboratory, 1 Cyclotron Rd., Berkeley, 94720 California, USA*

* csutterfella@lbl.gov

Keywords: Halide perovskites, in situ characterization, multimodal, synchrotron X-ray, optical properties, photoluminescence, absorption spectroscopy, reflectometry, crystallization kinetics

Abstract:

This chapter describes the application of in situ characterization to the synthesis of halide perovskites to understand formation pathways and gain mechanistic insights into thermodynamically and kinetically driven processes during perovskite film formation. The main techniques discussed are in situ X-ray and optical spectroscopy characterization.

9.1 Introduction

Material synthesis, including the fabrication of halide perovskites, is a fundamental aspect to discover and deliberately tailor new functional materials for energy applications.[1,2] To this end, the majority of characterizations are focused on post characterization of the perovskite material, often near equilibrium, or via implementation in optoelectronic devices coupled to device characterization. In situ measurements in contrast to ex situ measurements (also referred to as "black box" synthesis) enable the direct characterization of chemical transformations of the reagent to the product in real time during the reactions (**Figure 1**).[3–7] Here, in situ characterization refers to observing a process while it is taking place, whereas ex

situ characterization refers to measurements after the process is finished. For instance, in situ characterization of a perovskite thin film can provide information about the temporal evolution of crystal phases or optical properties.[8–10] In addition, it can reveal thermodynamic and kinetically-driven formation pathways as well as the potential formation of metastable phases.[4,7,11] The possibly intricate interplay between these driving forces during synthesis can influence the evolution of functional properties and consequently device operation. Hence, deliberate design of halide perovskites, and materials in general, can be facilitated by knowing how a material evolves and then manipulating its synthesis.

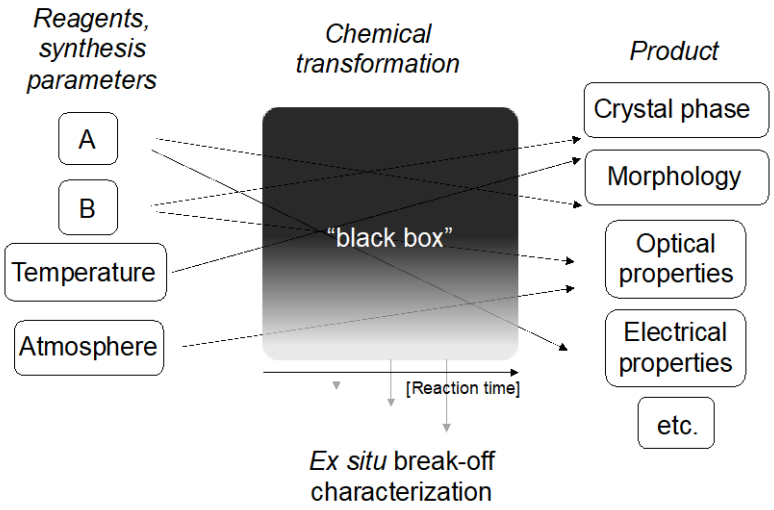

Figure 1 Schematic illustration of a "black box" synthesis with known reagents and synthesis parameters. Interrupting the chemical transformations at various points in time can provide snapshots during the transformation of reagents into the final product and are shown as ex situ break-off characterization. Modified from Ref.[3]

One prerequisite to capture the fast evolution of features during the solution deposition and consecutive annealing of halide perovskites is fast data collection i.e. fast detectors with ~ms or faster integration times and high-flux beam sources (such as X-rays). Technical developments over the last decade or so now allow for the in situ characterization of soft materials including their growth kinetics, meaning evolution of properties over time, and structural transformations.

One step further, in situ multimodal characterization is needed to correlate the evolution of functional properties such as bandgap and crystal phase, over time during synthesis.[3] These mechanistic insights will guide the choice of synthesis parameters in order to efficiently design syntheses and significantly increase reproducibility. In the past years, in situ and multimodal characterization of halide perovskites have gained significant interest and provided novel insights to advance the field. Lastly, in an endeavor to close the loop between synthesis, characterization, and computation, in situ characterization is one stepping stone towards synthesis automation and continues to gain momentum and experimental implementation.

In this chapter, the in situ characterization of halide perovskites will be briefly discussed via synchrotron-based X-ray scattering and fluorescence, optical spectroscopy, and the simultaneous combination of different techniques (multimodal characterization). The information one can extract from each technique will be exemplified on recent literature studies. Since in situ characterization is not a common characterization mode, many setups are custom build which will be described briefly. At the end, probe beam-sample interactions and considerations will be discussed followed by a summary and outlook.

9.1 Fundamentals of X-ray Scattering and Fluorescence Techniques

In this section, we provide a short review of the fundamentals of X-ray scattering and X-ray fluorescence techniques used for the in situ characterization of perovskite thin films. Firstly, we cover the fundamentals of grazing incidence wide-angle X-ray scattering (GIWAXS) and grazing incidence small-angle X-ray scattering (GISAXS), and their applications to probe the crystallization behavior at the small-length-scale ranging from Angstrom (Å) to a few nanometers (nm), and the perovskite grain formation. Then, we briefly provide fundamentals of X-ray fluorescence (XRF) and its application in probing the compositional evolution during film formation. The major focus based on its frequent application to halide perovskites is on GIWAXS. At the small-length-scale, GIWAXS can provide valuable information about the crystal packing structure, the orientation with respect to the device architecture, the relative degree of crystallinity, materials composition, and the crystalline correlation length (i.e. a parameter

related to the average size of perovskite crystals).[7,12,13] GISAXS makes use of the contrast between domains of different phases (either amorphous or crystalline) to give information about the average domain size.[12,13] Both lab-based and synchrotron-based X-ray scattering techniques have been used for perovskite thin film characterization, however, lab-based X-ray measurements are limited to static characterizations due to low photon flux and intensity of the X-ray beam requiring long measurement times.[14] On the other hand, synchrotrons provide intense and collimated X-ray beams with high photon flux allowing for the in situ characterization of fast film formation kinetics.[14]

9.1.1 Grazing Incidence Wide-angle X-ray scattering (GIWAXS)

Polycrystalline thin films with random crystal orientation may result in low peak intensities due to short X-ray path lengths in the thin film under symmetric diffraction conditions such as in Bragg-Brentano geometry (θ–2θ). To increase the X-ray path length and thus the resulting signal, grazing incidence X-ray diffraction (GIXRD) is used where the incoming X-ray angle is fixed at a shallow angle while the detector is moved. A portion of the beam is diffracted by the periodic crystallographic planes and diffraction occurs when Bragg's law is satisfied, as represented in Equation 1 below.[17] GIWAXS is focused on analyzing the Bragg diffraction at wide angles using high-energy (or hard) X-rays in the grazing incidence geometry. **Figure 2** illustrates the X-ray diffraction condition and grazing incidence geometry of a WAXS experiment. As shown in **Figure 2**a, the construction of reciprocal space and Ewald's sphere is used for predicting crystallographic scattering patterns.[17] Construction of reciprocal space relies on representing the parallel crystallographic planes in real space (green lines) as points in reciprocal space (green dots) where each point corresponds to a set of lattice planes labeled with Miller indices (*hkl*). The magnitude of the reciprocal space vector ($\vec{q}$) is defined by the inter-planar spacing of the lattice planes as $q = 2\pi/d$ and its direction is normal to the lattice planes. A sphere with a radius related to the wavelength of the incident X-ray beam via $2\pi/\lambda$ (equivalent to the magnitude of incident and diffracted beam vectors [$\vec{k_i}$ and $\vec{k_o}$, respectively]) is used to construct the Ewald sphere. Thus, all the possible incident and diffracted vectors are

hold by the Ewald sphere. The origin of the reciprocal space is the intersection of the incident beam at the edge of the Ewald sphere. The Bragg law is satisfied when reciprocal lattice points intersect the Ewald sphere, so that diffraction occurs (**Figure 2**) and Equations (1) and (3) are fulfilled.

$$2d_{hkl}\sin(\theta) = n\lambda \qquad (1)$$

$$\vec{q} = \vec{k_o} - \vec{k_i} \qquad (2)$$

$$q = \frac{2\pi}{d_{hkl}} = \frac{4\pi\sin(\theta)}{\lambda} \qquad (3)$$

Here, d_{hkl} is the spacing of the periodic planes *hkl*, 2θ is the diffraction angle, n is the order of reflection [n =1,2,3,..], λ is the X-ray wavelength, and $\vec{q}$ and q are the scattering vector and its magnitude, respectively.

Electronic and optoelectronic properties of perovskites are highly affected by their crystal structure hence the electronic band structure (or band structure) and its calculations rely on the periodic nature of a crystal lattice. These properties can show anisotropy along different crystallography planes, especially in the case of 2D perovskite structures. Therefore, determination of the texture or the crystallographic lattice orientation distribution is crucial for understanding the correlation between the microstructure and optoelectronic properties of perovskite thin films. GIWAXS is the most common methodology to investigate the texture orientation which can be revealed by the shape and polar distribution of the scattering peaks in a reciprocal space map as represented schematically in **Figure 2c** from left to right**:** (i) Pronounced Bragg diffraction peaks along the q_z direction appear when crystallographic planes are oriented perfectly parallel to the substrate corresponding to stacking out-of-plane. (ii) Partial arcs appear when the Bragg diffraction broadens as for crystallites with more distributed texture orientations, where crystallographic planes have angular distribution about the substrate surface. (iii) Full scattering rings similar to powder-like diffraction patterns are obtained for crystals randomly oriented in all directions. These schematics are only for one set of crystallographic planes. In a 3D lattice, there will be multiple peaks from different crystallographic planes. For instance, the diffraction pattern of the 2D perovskite $(PEA)_2PbI_4$ in

Figure 2b shows two sets of highly oriented diffraction peaks in the out-of-plane (q_z) and in-plane (q_{xy}) directions corresponding to crystallographic planes oriented parallel and normal to the substrate, respectively. Notably, partial arcs appear along the out-of-plane direction revealing an angular distribution about the substrate surface.

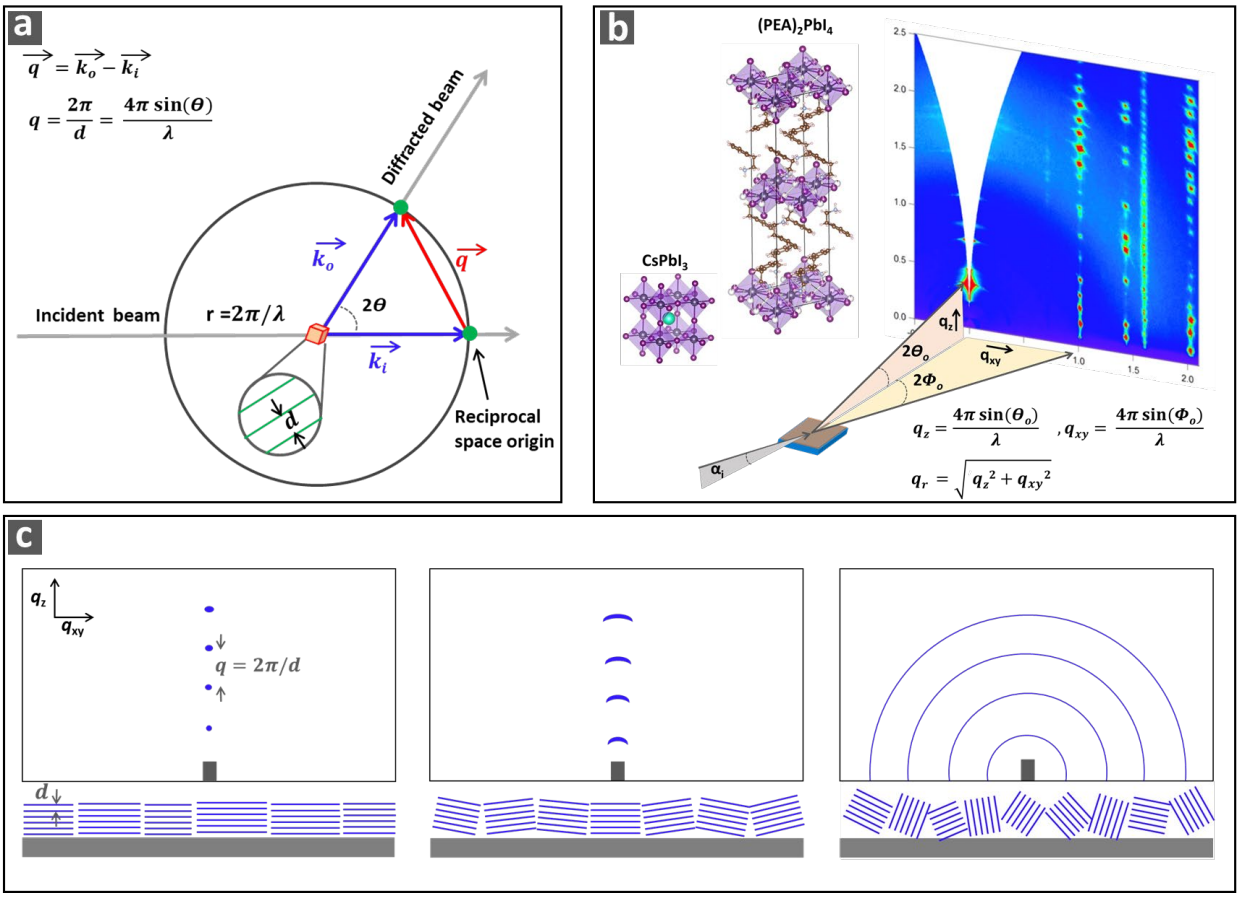

Figure 2 (a) Schematic representation of the X-ray diffraction condition. The reciprocal-space, calculated from the Fourier transform of the crystallographic planes in Euclidean space (green parallel lines) is represented as green dots. The circle represents the Ewald sphere with radius = $2\pi/\lambda$ and contains all wave-vectors of the incident and diffracted X-ray beams (k_i and k_o, respectively). (b) Schematic illustration of GIWAXS patterns for crystals with different texture orientations. The out-of-plane scattering (q_z) related to its scattering angle ($2\theta_o$) and the in-plane scattering (q_{xy}) related to its scattering angle ($2\Phi_o$) are shown as well as the calculation of the radial distance (q_r). The diffraction pattern corresponds to GIWAXS of the 2D perovskite $(PEA)_2PbI_4$. (c) Exemplary diffraction patterns corresponding to crystallographic planes oriented parallel to the substrate (left pattern), oriented with an angular distribution around the horizontal alignment (middle pattern), and randomly oriented in all directions (right pattern). Adapted with permission from Refs.[15,16]

9.1.2 Grazing Incidence Small-angle X-ray Scattering (GISAXS)

The GISAXS technique makes use of the difference in the refractive index that arises from inhomogeneities in the electron density of materials/phases depending on their mass density and elemental composition.[14,18] Large-scale inhomogeneities are expected to be present during film formation due to the evolution of different phases such as the perovskite phase, the intermediates, the amorphous phase, or a combination thereof. For instance, in situ GISAXS can be used to quantify the average domain size of emerging phases during film formation.[19,20] Moreover, SAXS can be applied to liquid samples to investigate the aggregation in solution. [7]

9.1.3 X-ray Fluorescence (XRF)

XRF can provide chemical information via the emission of characteristic X-rays and relies on the interaction and ionization of atoms by X-ray radiation. Ionization of atoms i.e. the removal of an electron may occur upon X-ray exposure if the radiation energy is larger than the respective ionization energy.[21] As a consequence, the electronic structure of the atom becomes unstable and electrons from higher orbitals will fill the inner state. This transition will release a photon with a characteristic energy for the atom involved corresponding to the energy difference between the two involved orbitals. Since the energy of the fluorescent radiation is characteristic of a transition between specific electron orbitals in a particular element, the resulting fluorescent X-rays can be used to detect the presence of elements during film formation.[6] The relative amount of different elements can be deduced from their relative XRF intensity.[6]

9.1.4 Selected Examples for in Situ X-ray Scattering and Fluorescence

In this section, we provide a few selected examples of deploying X-ray characterization techniques in an in situ mode to probe the synthesis of halide perovskite thin films.

9.1.4.1 In Situ GIWAXS to Study Crystallization Kinetics and A-site Doping

Qin et al. used in situ GIWAXS to investigate the crystallization pathways of a two-step-fabricated $FAPbI_3$ perovskite thin film with sequential A-site doping of Cs^+ and GA^+.[4] Typically, in

the two-step process a PbI_2 layer is fabricated first, followed by its conversion to perovskite in the second step via the deposition of organic salts (e.g. formamidinium iodide, methylammonium bromide, and/or methylammonium chloride dissolved e.g. in isopropyl alcohol) and interdiffusion of PbI_2 and the organic salts during heat treatment. Qin et al. modified this process by introducing CsI and guanidinium iodide (GAI) into the precursors for the first and second deposition steps, respectively. They found that the addition of CsI alters the crystallization pathway during the first step. In the presence of CsI, the δ-$CsPbI_3$ phase was observed during spin coating together with a weak signal from hexagonal PbI_2while in the absence of CsI, PbI_2 only appears during the annealing step. It was concluded that incorporation of Cs^+ leads to the co-existence of δ-$CsPbI_3$ and PbI_2 phases, and that PbI_2 growth is likely a thermally activated process in this system. Then, focusing on the second synthesis step, variations in the crystallization pathway were found depending on the presence of Cs^+ and GA^+. **Figure 3** shows the integrated scattering intensity, the 2D GIWAXS intensity plots for the evolution of $FAPbI_3$ with Cs^+ and GA^+, and the time evolution of peak areas of δ-$CsPbI_3$, PbI_2, and perovskite phases. For the reference sample without Cs^+ or GA^+, only three stages can be identified while in the case with Cs^+ and GA^+, four stages were found. Stage I contains the PbI_2 and δ-$CsPbI_3$ phases, Stage II shows the perovskite α-phase formation and a decay of both PbI_2 and δ-$CsPbI_3$ phases. In Stage III, the transition from the δ-$CsPbI_3$ phase to the perovskite phase continues with a much slower transition rate than in Stage II and it ends by the disappearance of the δ-$CsPbI_3$-phase peak. Stage IV is characterized by further crystallization of pure perovskite α-phase until saturation. While both Cs-doped and Cs+GA-doped syntheses have four similar stages, GA^+ induces an accelerated phase transition from δ-$CsPbI_3$ to the perovskite phase. For Cs-doped films, pinholes form due to the non-uniform nucleation with sparse δ-$CsPbI_3$ crystals. Fortunately, for Cs+GA-doped films, incorporating GA^+ in the second step helps to eliminate pinholes via Ostwald ripening and enhanced grain boundary migration.

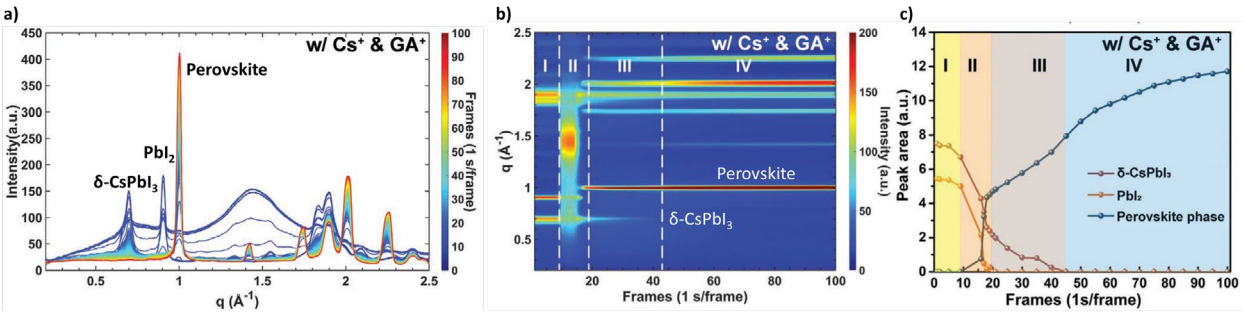

Figure 3 (a) GIWAXS integrated scattering intensity and (b) False-color 2D GIWAXS intensity maps showing *q* versus time (frame number) for the second step of a two-step-fabricated $FAPbI_3$-based perovskite with Cs^+ and GA^+. (c) The time evolution of peak areas of PbI_2, δ-$CsPbI_3$, and perovskite phases. Adapted with permission.[4]

9.1.4.2 In situ GIWAXS to Probe Film Evolution via Antisolvent and Gas Jet Treatments

Typical engineering strategies to induce crystallization during the fabrication of halide perovskites include antisolvent dripping and N_2 gas jet treatment during spin coating.[7,22] In a study by Abdelsamie et al., in situ GIWAXS was used to provide fundamental understanding of the crystallization processes to form $Cs_{0.15}FA_{0.85}PbI_3$ via antisolvent-assisted synthesis or N_2 treatment (schematic illustration **Figure 4**a).[7] In particular, this study extracted phase fractions from the in situ data to reveal compositional fluctuations during synthesis. It was found that when applying N_2, the initial crystallization of the hexagonal non-perovskite (δ_H) $FAPbI_3$ crystallites occurred after an incubation period and were found to be highly oriented in the out-of-plane direction along q_z, followed by crystallization of more randomly oriented crystallites. As depicted in **Figure 4**a, applying N_2 accelerates the solvent removal from the air–liquid interface while the lower region of the film reaches supersaturation after an incubation period and crystallization starts from the top surface. The initial formation of highly oriented crystallites was attributed to vapor-interface-induced crystallization while homogeneous crystallization occurs at later times in the bulk solution in addition to the vapor-interface-induced crystallization. On the other hand, when dropping CB, both, the initial and later δ_H-$FAPbI_3$ crystallization exhibited relatively broader orientation compared to the N_2-treated films, revealing a more dominant isotropic crystallization taking place in the bulk of the wet film. As represented in **Figure 4**a, when dropping the antisolvent CB, rapid diffusion of CB into the bulk

occurs leading to immediate supersaturation and relatively more homogeneous crystallization without an incubation period, compared to applying N_2. Quantitative analysis of the compositional evolution during thermal annealing was revealed through deconvolution of the contribution of thermal expansion and compositional evolution to the observed shift of the (100) peak position of the perovskite phase (referred to as α-phase, **Figure 4**b). Furthermore, the evolution of the volume fractions of α-phase, δ_H-phase, and amorphous phase was calculated from the intensity evolution of the δ_H- and α-phase peaks during thermal annealing using Equation 4, below.[23]

$$I \propto \left(\frac{I_0\,\lambda^3}{16\pi d}\right)\left(\frac{e^4}{m_e^2\,c^4}\right)\left(\frac{V\,m^{hkl}\,(F^{hkl})^2}{v^2}\right)(LPF) \quad \text{, where} \quad LPF = \left(\frac{\alpha_{polarization}}{\sin(\theta)\sin(2\theta)}\right) \tag{4}$$

Here, I is the integrated scattering intensity from a reflection hkl, I_0 is the incident intensity of the radiation beam, λ is the X-ray wavelength, d is the sample to detector distance, e is the electron charge, m_e is the electron mass, c is the speed of light, V is the diffracting volume, m^{hkl} is the multiplicity of a reflection hkl, F^{hkl} is the structure factor of a reflection hkl, v is the volume of the unit cell , and LPF is the Lorentz polarization factor, $\alpha_{polarization}$ is the polarization correction factor, and 2θ is the diffraction angle.

Interestingly, the films exhibited an inhomogeneous distribution of Cs and FA in the as-cast films with the segregation of Cs in the α-phase (with ≈ 30-35 at% Cs) and FA in the pure δ_H-$FAPbI_3$ (see **Figure 4**b at the start of the annealing). During subsequent annealing, cation (Cs, FA) diffusion occurs leading to the formation of a more homogenous microstructure with an average stoichiometry of ~15 at% Cs, $Cs_{0.15}FA_{0.85}PbI_3$, while crystallization of the α-phase occurs at the expense of the δ_H-$FAPbI_3$ and the amorphous phase simultaneously (**Figure 4**c). The evolution of phase fractions revealed different crystallization behavior for the different synthesis conditions. Crystallization of perovskite α-phase occurred predominantly from amorphous phase rather than from a crystalline precursor in the sample without antisolvent or N_2 treatment. On the other hand, crystallization occurred predominantly from a more crystalline precursors when applying CB or N_2 during spin coating. The latter was linked to obtaining a smoother morphology and fully covering perovskite thin films because the more

crystalline precursor in the as-cast films possibly dictates the growth of perovskite phase during thermal annealing.

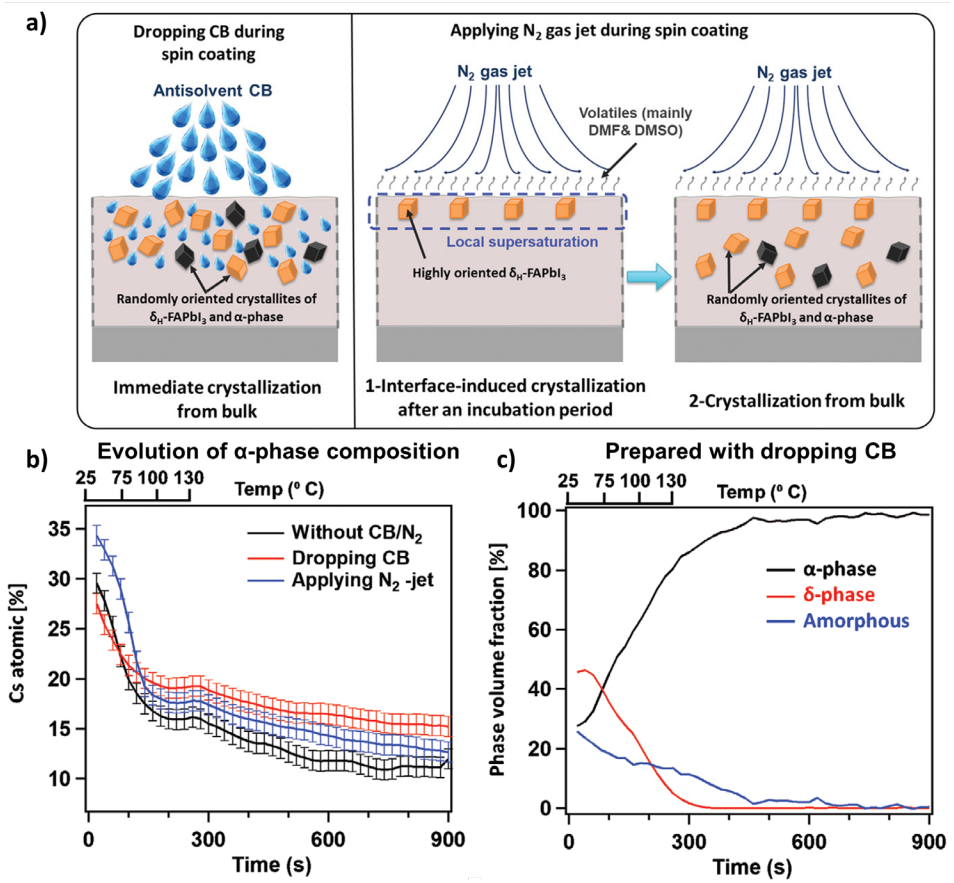

Figure 4 (a) Schematic representation of the mechanism of dropping antisolvent (left) and applying N_2 gas jet (right) during the spin coating step. (b) Time evolution of the α-phase composition during thermal annealing of $Cs_{0.15}FA_{0.85}PbI_3$ treated with antisolvent or N_2 and the reference after spin coating. (c) Time evolution of the calculated phase volume fraction of α-phase (black line), δ_H-phase (red line), and amorphous phase (blue line) for films prepared by dropping an antisolvent (chlorobenzene, CB). Adapted with permission.[7]

9.1.4.3 In situ X-ray diffraction (XRD), XRF, and GISAXS to Probe the $PbCl_2$-derived Formation of $MAPbI_3$

Stone et al. used a combination of in situ XRF and X-ray diffraction (XRD) to gain information on elemental changes and phase formation, respectively, during the formation of $PbCl_2$-derived $MAPbI_3$ from precursors containing $PbCl_2$ + 3 MAI (MA = CH_3NH_3).[6] This combination of in situ techniques allowed to understand the transformation chemistry from the liquid precursor to

the solid perovskite phase (summarized in **Figure 5**c). In-situ GIXRD during subsequent annealing revealed that the crystallization pathway goes through an intermediate stage where the peaks corresponding to the Cl-containing crystalline precursor phase (MA_2PbI_3Cl) remain nearly constant with no observable perovskite formation (**Figure 5**a). This stage is followed by a transformation stage characterized by continued loss of MA_2PbI_3Cl concurrent with the growth of the perovskite phase. For all temperatures investigated, in situ XRF measurements revealed a linear decay of Cl (**Figure 5**b). This behavior was attributed to the desorption of MACl from a constant surface area, apparently from the MACl disordered phase in the film. Furthermore, no perovskite crystallization occurs until the removal of 50% of Cl, see the onset of perovskite crystallization in **Figure 5**b. Hence, the precursor transformation to perovskite only happens after the disordered MACl phase has evaporated (schematic **Figure 5**c).

Another study relied on small angle scattering measurements via in situ GISAXS to complement wide angle characterization down to *q* values of 10^{-3} $Å^{-1}$ (corresponding to length scales as large as 400 nm in real space). [20] At thermal annealing at 80 °C a gradual intensity increase in *q* value was observed and it was concluded that as the perovskite film forms there is an increase in the fraction and number of structures that range from 30-400 nm in size.

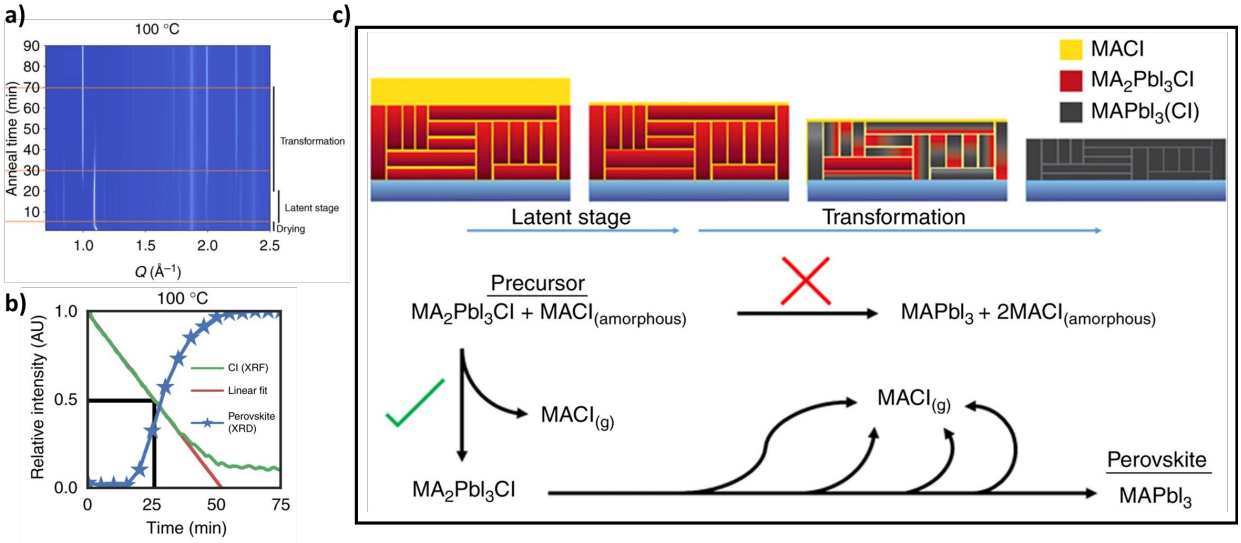

Figure 5 (a) In situ XRD of the PbCl2-derived MAPbI3 while annealing at 100 °C. b) Relative amount of Cl (from XRF) and crystalline perovskite (from GIXRD) while annealing at 100 °C. (c) Schematic representation of the transformation from a PbCl2-derived precursor to perovskite phase. Adapted with permission.[6]

9.1.4.4 In situ GIWAXS to probe the 2D/3D Interface formation

A successful strategy to passivate perovskite thin films is via the incorporation of thin 2D or quasi-2D perovskite layers. The formation of the 2D/3D interface is typically done via solution processing where the 2D perovskite layer is deposited onto the fully fabricated 3D perovskite film. To provide mechanistic insights into the 2D/3D interface formation, in situ GIWAXS was measured during spin-coating.[24] In this example a VBABr-based (VBA = vinylbenzylammonium) 2D perovskite was deposited on top of $MAPbI_3$ and $(MAPbBr_3)_{0.05}(FAPbI_3)_{0.95}$ films. In situ GIWAXS has provided insight into both the crystal structure and the orientation of evolving phases during the 2D/3D interface formation (**Figure 6**). The as cast $MAPbI_3$ and $(MAPbBr_3)_{0.05}(FAPbI_3)_{0.95}$ films show scattering from 3D perovskite and PbI_2 crystals as shown in the GIWAXS patterns at t = -6s and t = -7s in **Figure 6**a and **6**d, respectively. For $MAPbI_3$, an intermediate state with higher q (≈ 0.50 Å^{-1}) than any VBA-based 2D structure is observed before n=1 of the 2D phase $(VBABr)_2MA_{n-1}Pb_nI_{3n+1}$ is formed. The intermediate state was attributed to 2D PbI_2 sheets intercalated by IPA solvent molecules, marked as i-PbI_2 in **Figure 6**a. On the other hand, 2D/3D interface formation for $(MAPbBr_3)_{0.05}(FAPbI_3)_{0.95}$ occurs via a progressive reduction of dimensionality from n=3 to n=1 of the 2D structure $(VBABr)_2(FA_{0.95}MA_{0.05})_{n-1}Pb_n(I_{0.95}Br_{0.05})_{3n+1}$, rather than the immediate formation of n = 1 (**Figure 6**c-d). In both cases, the diffraction peaks of the VBA-based 2D structures are highly oriented in the out-of-plane direction with arc-like scattering indicating oriented 2D structures parallel to the substrate with an angular distribution around the horizontal alignment. The difference in the 2D/3D interface formation pathways was attributed to differences in the stability between $MAPbI_3$ and $(MAPbBr_3)_{0.05}(FAPbI_3)_{0.95}$ films, where the less stable $MAPbI_3$ is more prone to conversion to PbI_2, thus forming intermediate PbI_2-intercalated phases with the solvent molecules. Moreover, density functional theory (DFT) calculations suggested that the VBA-ligands infiltrate the 3D perovskite layer leading to splitting of the 3D perovskite phase to

lower-dimensional fragments that continuously split till forming $n = 1$, supporting the observations of in situ GIWAXS results. The formation of higher n 2D structures was hypothesized to occur initially but their (001) diffraction peaks have too low q to be observed in the GIWAXS experiments in the study.

In situ GIWAXS was also used during heating to characterize the evolution of the 2D/3D interface and to reveal the role of 2D perovskites (2-TMAI or PEAI) in inhibiting degradation.[10] The in situ GIWAXS results revealed the transformation of the 2D crystalline structure into a mixed 2D/3D phase leading to blocking the degradation of the 3D bulk into lead iodide and keeping the 3D bulk underneath intact. These results provided guidelines for engineering stable device interfaces.

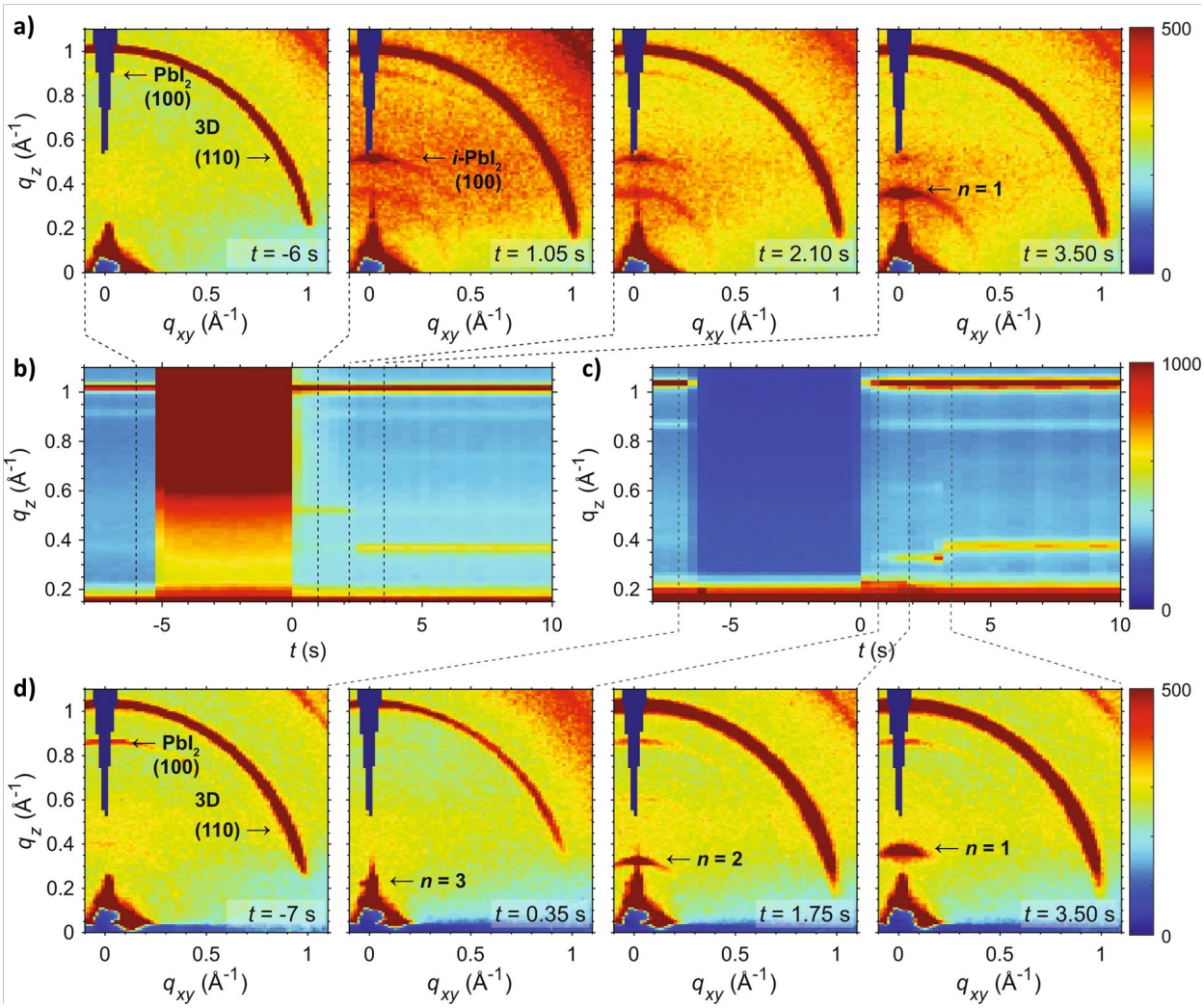

Figure 6 (a) 2D GIWAXS patterns for a $MAPbI_3$ film treated with a solution of 5 mg/mL VBABr in IPA. The intercalated PbI_2 peak is marked as i-PbI_2. (b) False-color 2D GIWAXS intensity maps showing *q* versus time during spin-coating of VBABr solution on $MAPbI_3$ films. (c) False-color 2D GIWAXS intensity maps showing *q* versus time during spin-coating of 1 mM VBABr in 3:97 IPA:CF solution on $(MAPbBr_3)_{0.05}(FAPbI_3)_{0.95}$ films. Time zero in (b-c) is the start of spin-coating. (d) 2D GIWAXS patterns for $(MAPbBr_3)_{0.05}(FAPbI_3)_{0.95}$ films treated with VBABr solution. Adapted with permission.[24]

9.2 In situ Optical Spectroscopy

This section briefly deals with the UV-Vis-NIR optical spectroscopy highlighting the interaction of electromagnetic waves with perovskite materials resulting in absorption, transmission, reflection, and/or emission. More in depth discussion of the photophysical processes in halide perovskites will be addressed in Chapters 13 and 19. Here, the transmission

and reflection of light are briefly covered followed by photoluminescence emission and its application in the in situ characterization of halide perovskite synthesis. Several application examples and information obtained on phase evolution and formation kinetics are discussed.

9.2.1 Fundamentals of Absorption and Emission of Light in Halide Perovskites

Optical spectroscopy plays a key role in the characterization of the optical properties and probing the photophysical processes occurring in halide perovskites. **Figure 7**a illustrates the photophysical processes occurring in halide perovskites after the absorption of a photon with an energy higher or equal to its bandgap energy. The absorbed photon creates free charge carriers or a quasiparticle (electron-hole pair or exciton). It is suggested that free charges are the primary species after photoexcitation in halide perovskites.[25] The excitons in halide perovskites are reported to be Wannier-Mott excitons where the electron is weakly bound to the hole and excitons are free to move in the material.[26] Many studies report exciton binding energies (E_b) of a few tens of meV and fast dissociation (<1 ps).[25–27] When applying in situ optical characterization during synthesis and in particular during the annealing of halide perovskites, the supplied thermal energy (26 meV at room temperature and 32 meV at 100 °C) may be sufficient to dissociate the excitons. Photon-generated free charges are mobile and carrier diffusion lengths between 100 nm to a few micrometers have been found at room temperature (in the low carrier injection regime).[25] Ultimately, free charges if not collected at the electrodes will recombine, either non-radiatively or radiatively. Depending on the nature and density of trap states, trapping and de-trapping can occur.

Halide perovskites show strong light absorption with a sharp optical absorption edge and absorption coefficients >10^4 cm^{-1} above the bandgap.[29] The light absorption properties can be characterized by wavelength-dependent absorbance (A_λ) measurements where $A_\lambda = -log_{10}(T_\lambda)$ with the transmitted radiation T_λ. Performing in situ transmission measurements during synthesis is useful to analyze optical features that relate to the band structure such as the absorption edge and its evolution during synthesis (more in Chapter 9.2.3). Photoluminescence (PL) or radiative recombination of electrons and holes is the spontaneous emission of light under optical excitation. For instance, the absorption edge for

$MAPbI_3$, calculated from PL and transmittance measurements, shifts monotonically to higher energies with increasing temperature (**Figure 7**b). This behavior is opposite to other tetrahedrally coordinated semiconductors (such as silicon and gallium nitride) and is explained by a reverse band edge electronic states ordering.[30] In general, with increasing temperature, impurities as well as excitons become ionized. As a consequence, photoexcited free charges increasingly populate the conduction and valence band leading to an increasing probability for band-to-band transitions. Spectrally resolved room temperature PL of halide perovskites results in a broad peak. In first approximation, the maximum of the PL emission peak energy can be interpreted as the bandgap of the sample.[31] In addition, the peak position can be used for compositional analysis via correlation with the bandgap of the perovskite material.

Other features of PL spectra include the peak intensity and width (usually characterized by its full width at half maximum [FWHM]). The PL FWHM characterizes the broadening of PL peaks, which may be caused by thermal effects, bandgap fluctuations, and the population of discrete states. Typically, a high PL intensity is correlated with high quality materials. During synthesis and in particular during the thermal annealing stage, the PL intensity exhibits convoluted dependencies. It is influenced by trap states and complicated temperature dependent recombination dynamics and rates, thermal quenching which has been explained by thermally activated exciton dissociation, as well as quenching as a result of phonon-assisted non-radiative recombination and thermally activated carrier trapping.[26,32] Generally, a red shift is observed between the band-edge absorbance and PL spectra, referred to as Stokes shift (**Figure 7**b). As shown for $MAPbI_3$ in **Figure 7**b, the observed shift is nearly constant and its magnitude is ~ 4-6 meV and ~ 11-12 meV in the tetragonal and cubic phase, respectively.[28] As a last comment, synthesis often involves a room temperature deposition followed by a thermal annealing step, which in the case of the prototype $MAPbI_3$ involves a crystal structure change from tetragonal to cubic around 310K (**Figure 7**b).

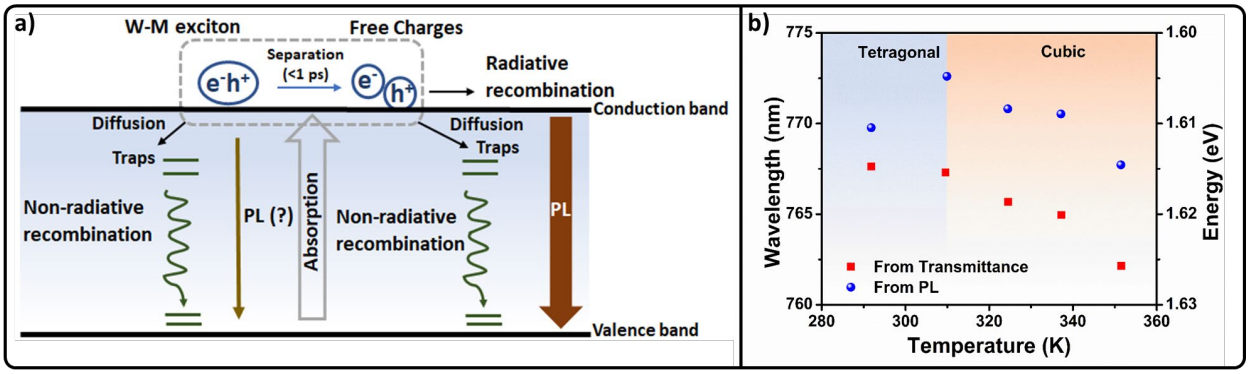

Figure 7 (a) Schematic of the photophysical processes in halide perovskites. (b) PL peak energy and absorption band edge as a function of temperature for $MAPbI_3$. Blue = tetragonal phase, orange = cubic phase. Data is extracted and replotted from Ref.[28]

9.2.2 Setup Design for in Situ Optical Spectroscopy

There are a few key components required to run the most basic PL and UV-Vis absorbance measurements, namely, a light source (monochromatic in the case of PL) and a spectrometer (**Figure 8**).[31] More advanced setups include for example filtering and focusing optics, objectives, and motorized stages.[33] Application of in situ spectroscopy measurements during halide perovskite synthesis typically involve the characterization during deposition and thermal annealing. For in situ PL, since halide perovskites exhibit high luminescence quantum yield, low power class lasers or light emitting diodes with narrow emission spectrum (e.g. class 3R, output power < 5mW) can often be sufficient to characterize synthesis. Consequently, low light source hazards might enable the direct implementation of PL optics into a typical synthesis environment such as a glovebox (**Figure 8**). Upon excitation, the PL signal is collected by the collection optics which are commonly fiber coupled to a spectrometer. In the spectrometer, the signal is spectrally resolved and guided to a detector array. Short acquisition times are required to resolve fast dynamic changes during halide perovskite synthesis especially during the application of solution engineering strategies such as antisolvent dripping during spin coating and early during thermal annealing. The minimum acquisition time strongly depends on excitation energy and density, quantum yield of the sample, as well as setup related specifications. Sub-second acquisition times can be achieved using an incoming photon flux similar to the 1-sun AM 1.5 spectrum. In situ UV Vis transmission and reflection measurements,

require a white light source, some collection optics, and a spectrometer. The advantage of performing in situ measurements in a real processing environment is the application of findings to typical halide perovskite fabrication processes since the majority of thin films is made via spin coating and annealing in a glovebox with controlled atmosphere.

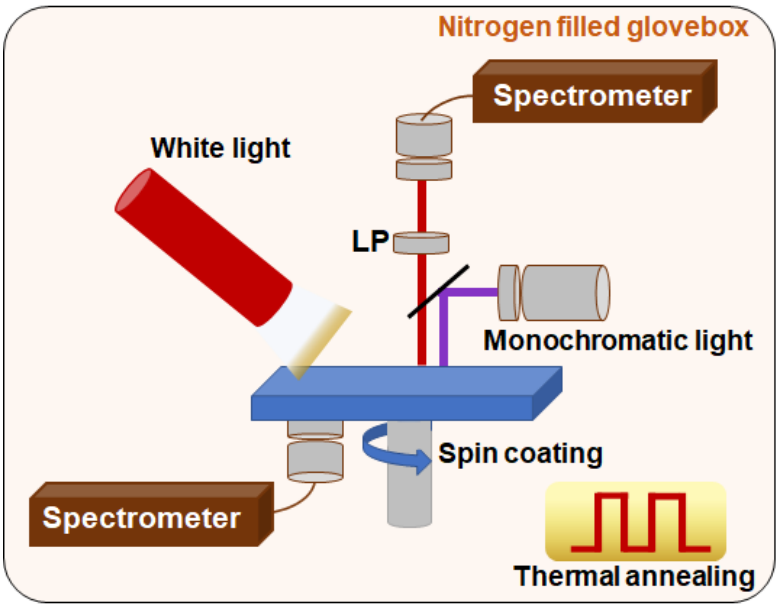

Figure 8 Schematic illustration of in situ spectroscopy setups installed in a synthesis glovebox showing in situ transmission and photoluminescence performed during spin coating and heating.

9.2.3 Selected Examples for In Situ Optical Spectroscopy

In this section, we provide a few selected examples of optical spectroscopy characterization techniques in an in situ mode to probe halide perovskite thin films synthesis.

9.2.3.1 Fast In Situ Reflectance Measurements to Characterize the Perovskite Formation

In a recent study, fast in situ optical reflectance measurements were used to characterize the spin coating and annealing of different halide perovskite compositions including

($CH_3NH_3PbI_3$, MAPI), ($CH_3NH_3PbBr_3$, MAPBr), ($HC(NH_2)_2PbI_3$, FAPI), and the triple cation perovskite (TripleCat) $Cs_{0.05}(FA_{0.83}MA_{0.17})_{0.95}Pb(I_{0.83}Br_{0.17})_3$.[34] Reflectometry measures reflected light and depends on the absorption coefficient, refractive index, and scattering processes. The setup used is inside a glove box with a fiber coupled tungsten lamp. During spin coating the light was perpendicular to the film surface but 15° off-axis during annealing to collect diffuse scattered light. Integration times during spin coating were 0.2-0.5 ms and 10-40 ms during the annealing. The interference patterns and fringes from specular reflectance measurements collected during spin coating are illustrated in **Figure 9**. During the first few seconds of spin coating (t < 10 s), a fast spectral shift of the interference fringes is observed due to the initial ejection of the solution. At longer times (t > 10 s), the spectral shift of the fringes gets slow while the spectra appear with a lower number of fringes but with higher amplitude (red color in **Figure 9**a). At t > 28 s, the surface roughened and specular reflectance disappears and only diffuse light scattering can be measured (indicated as t_{end} in **Figure 9**a). The study found that t_{end} mainly depends on the solvent-ion interaction in solution and concluded that the complex formation energy is the lowest for $MAPbI_3$ and highest for triple cation precursors. The layer thickness (d) during synthesis (**Figure 9**c) was calculated using the interference fringes via:[35]

$$d = \frac{\lambda_1 \cdot \lambda_2}{2 \cdot [\lambda_1 \cdot n(\lambda_2) - \lambda_2 \cdot n(\lambda_1)]} \ , \lambda_1 > \lambda_2 \quad (5)$$

For the perovskite precursor solutions, the changes in dispersion of $n(\lambda)$ is small between 500 nm < λ < 1100 nm and is dominated by the solvent. Thus, Equation (5) can be simplified to Equation (6).

$$d = \frac{\lambda_1 \cdot \lambda_2}{2 \cdot n(\lambda_1 - \lambda_2)}, \lambda_1 > \lambda_2 \quad (6)$$

Here, λ_1 and $\lambda_2$correspond to wavelengths of two successive maxima or minima and n is the refractive index.

For all films, the wet film thickness initially decreases rapidly before it levels out after ~10 s. The TripleCat wet films exhibited a higher final thickness than the other precursor solutions (**Figure 9**c), which was attributed to a stronger interaction of the precursor ions with the

solvent molecules.[34] Furthermore, the in situ reflectance measurements during prolonged spin coating are used to gain insights into the extent of crystallization of the films. MAPI and FAPI films exhibited no reflectance features associated with perovskite formation while $FAPbI_3$ still showed interference patterns. In contrast, MAPBr and TripleCat films showed evolving reflectance features, which were interpreted as the development of the perovskite bandgap upon the solvent evaporation. These findings were supported by XRD measurements that have shown perovskite peaks for the as-cast MAPBr and TripleCat films, but not for the MAPI and FAPI films. Diffuse in situ reflectance measurements during the annealing were used to further characterize the perovskite formation. They revealed that perovskite formation occurs within ~7 s at 100 °C for MAPI but requires much longer time (~60 s) at 165 °C for FAPI. For MAPBr and TripleCat films, no significant changes were observed during annealing since the perovskite formation occurred during spin coating. Notably, since reflectometry cannot provide direct crystal phase information nor a precise energetic position of the bandgap, it would be a powerful combination to characterize perovskite synthesis with a combination of reflectance, diffraction and/or absorbance.

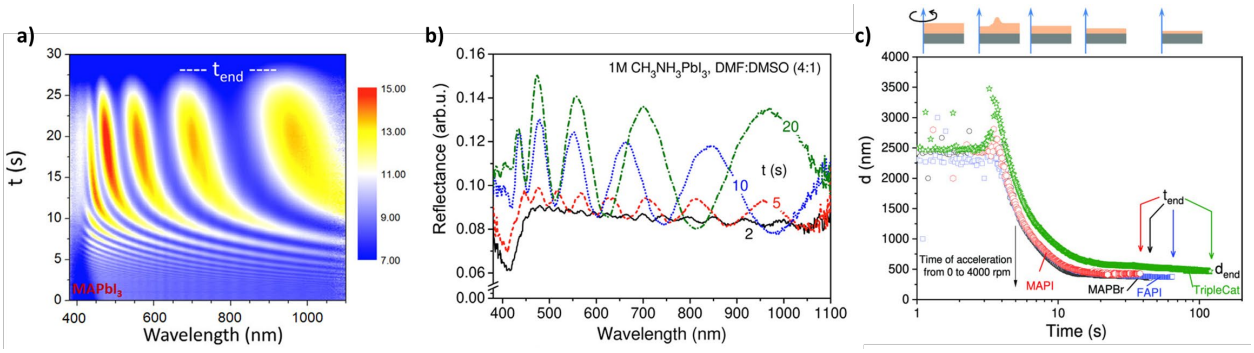

Figure 9 (a) Specular reflectance spectra (in %) as a function of wavelength over time measured during spin coating of $MAPbI_3$ precursor solution. (b) Individual reflectance spectra measured during spin coating at selected times, given in the figure. (c) Time-evolution of the layer thickness during spin coating of perovskite precursor solution; MAPI (red), MAPBr (black), FAPI (blue), and TripleCat (green). Adapted with permission from Ref.[34]

9.2.3.2 In Situ UV-Vis Absorbance Characterization During the Drying Stage

In an effort to scale up the solution process of halide perovskites, Hu et. al used laminar air-knife-assisted meniscus coating at room temperature.[5] To enable controlled drying kinetics during the liquid-solid transformation, in situ UV-Vis absorption spectroscopy was performed to establish correlations between supersaturation, nucleation, and growth rate. Two different drying processes, drying with natural air and with a laminar flow N_2 knife in a N_2 glovebox, were compared. For natural air drying, the in situ UV-Vis absorption measurements revealed three stages, marked as solution, intermediate, and solid stage in **Figure 10**a. In Stage I (solution), only the absorbance from the precursor solution (at $\lambda \leq 440–450$ nm) was observed. In the 2nd stage (intermediate), a gradual red-shifting of the absorbance edge is observed. The red-shifting was correlated to an increased precursor concentration upon solvent evaporation leading to nucleation and growth of the perovskite crystallites and/or solvent-containing intermediates (DMSO adduct).[36] In the 3rd stage (solid), stabilized absorbance is observed revealing the complete transformation of the precursor to solid perovskite. In contrast, when using the laminar N_2 knife, red-shifting in the absorbance spectra occurs ten times faster and saturation is reached almost instantly (**Figure 10**b). To quantify the wet film drying rate, the first derivative of the absorbance at 500 nm for the two drying processes was plotted (**Figure 10**c). It was found that using the laminar N_2 knife accelerates the solvent drying rate by two orders of magnitude compared to natural air drying and thus, enables controllable and fast perovskite film formation. The use of the laminar N_2 knife enabled rapid nucleation and high-quality films with compact and smooth morphology using a wide processing window (i.e., as long as applying N_2 knife in the solution state)

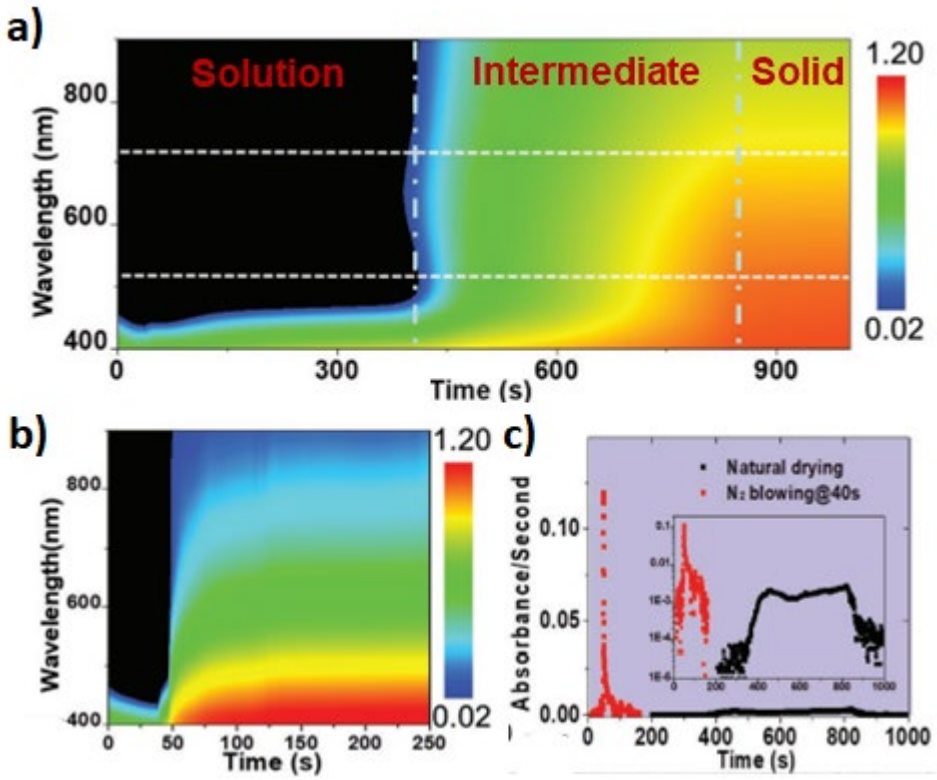

Figure 10 (a) Time-resolved contour plot of in situ UV-Vis absorbance spectra of natural air drying hybrid perovskite film. (b) Time-resolved in situ UV-Vis absorbance spectra of laminar air-knife-assisted meniscus coated nitrogen blowing. (c) The first derivative of the absorbance at 500 nm. Adapted with permission from Ref.[5]

9.2.3.3 In Situ Photoluminescence Characterization to Investigate the Role of the Precursor

A combinatorial in situ approach was used to investigate the role of the lead precursor on the physicochemical evolution of $MAPbI_3$ thin films using three different lead salts (PbI_2, $PbAc_2$, $PbCl_2$).[37] While a multimodal approach combining in situ PL, in situ XRD and in situ imaging was used, the main focus here is on the in situ PL (**Figure 11**). The benefits of multimodal in situ studies will be discussed in more detail in section 9.3. Song et al. measured PL deploying a home-built setup in the fume hood using a 532 nm laser diode as excitation source. They then fitted each individual PL spectrum using a single Gaussian and investigated both the time-evolution of the intensity and the peak position during thermal annealing (see **Figure 11**a). All three precursors exhibited a similar PL-evolution during annealing, however, the amplitude of the observed shifts of the PL peak positions, intensities, and kinetics strongly depend on the Pb-

salt. In all three cases, the initial PL signal occurs at a higher energy than the bulk bandgap energy of $MAPbI_3$ with an energy shift (ΔE). The magnitude of the observed shifts of the PL peak positions strongly depends on the Pb-salt. The halide salts (PbI_2 and $PbCl_2$) exhibited an order of magnitude larger energy shift ΔE than $PbAc_2$. **Figure 11** shows the result for PbI_2 as an example. During annealing, the PL position red-shifts to the position of bulk $MAPbI_3$ while the $PbCl_2$ precursor showed larger delay compared to the other two precursors. This initially blue shifted PL was attributed to a possible quantum-confined PL emission from small nanocrystallites while the red-shifting was attributed to the growth of the nanocrystallites.[38–42] Thus, the smaller ΔE for $PbAc_2$-derived precursors was hypothesized to be due to an increased initial size of the $MAPbI_3$ crystallites compared to Pb-halides. Notably, the red-shifting occurred much faster in the acetate case which was attributed to faster perovskite formation in agreement with other studies.[43] In situ diffraction measurements confirmed the immediate perovskite formation without intermediate phase in the case of $PbAc_2$-derived precursors (agreeing with the small ΔE). In contrast, crystallization in case of the Pb-halides-derived precursors occurred via the formation of a precursor-solvent complex leading to slower perovskite formation compared to the $PbAc_2$-derived precursors. Furthermore, all precursors exhibited double-maxima in the PL intensity during thermal annealing (see **Figure 11**a for PbI_2 case). Following their interpretation of nanocrystal-nucleation, the authors associate the first increase and drop of the intensity with an increasing volume density of nucleation sites upon supersaturation triggered by solvent-evaporation, while the second increase was attributed to perovskite crystal growth, followed by a monotonous intensity-decrease due to photo darkening effects. These findings show high sensitivity of in situ PL to subtle compositional and phase variations.

Another study used in situ PL as a fast tool to optimize the parameter space of annealing temperature and annealing time for the hot-casting of $PbCl_2$/$PbAc_2$-containing precursors.[44] Moreover, in situ PL was used to characterize the growth dynamics of chlorine-containing $MAPbI_{3-x}Cl_x$.[8] Relying on the extracted Urbach energy from in situ PL spectra, the defect density of the $MAPbI_{3-x}Cl_x$ was found to be very low during nucleation and initial growth but

significantly increased upon the formation of defective crystallite surfaces and grain boundaries.

The abovementioned findings demonstrate the potential of in situ PL as a fast non-destructive technique to monitor perovskite formation. As discussed later in section 9.4, there is however a rapid charge carrier funneling happening upon light excitation which might prevent the PL analysis from gaining full information.

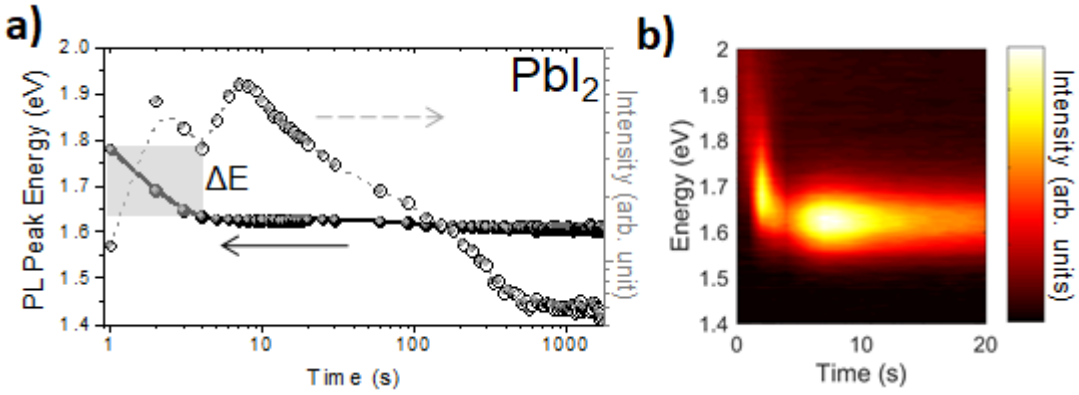

Figure 11 (a) Time-evolution of the PL peak position and intensity extracted from the individual PL spectra during thermal annealing of PbI_2-derived $MAPbI_3$ thin films. (b) 2D heat map of the corresponding PL measurements. Adapted with permission from Ref.[37]

9. 3 Examples of In Situ Multimodal Characterization During Solution Synthesis

As discussed in the sections above, in situ measurements can be a very powerful tool for monitoring the evolution of functional properties of perovskite materials during their fabrication process. Combining different, and ideally complementary, in situ techniques, referred to as multimodal characterization, can further improve mechanistic insights of how and when reagents are transformed into the final product. Thus, the additional value of multimodal characterization is a combination of functional characterizations that add up to more than the sum of their contributions due to the possibility to perform correlative analyses. In this section, two application examples of multimodal in situ characterization will be discussed, including a combination of two in situ optical techniques and combined in situ PL and synchrotron-based X-ray diffraction to unveil the formation of $MAPbI_{3-x}Cl_x$ and $MAPbI_3$ with particular focus on the antisolvent dropping step, respectively.

Combined in situ reflectometry and PL measurements were used to characterize a one-step deposition routine consisting of the spin-coating of a (MAI + $PbCl_2$):DMF precursor solution, drying of the spin-coated film, and subsequent annealing.[45] While previous studies confirmed the presence of chlorine in the precursor phases (e.g. MA_2PbI_3Cl) after spin-coating as well as a subsequent loss of MACl during annealing, the precise mechanism of the chlorine-loss and the incorporation of chlorine into the $MAPbI_{3-x}Cl_x$ thin film were not well understood., The evolution of the concentration of the chlorine-containing $MAPbI_{3-x}Cl_x$ phase in the thin film was extracted by applying a Beer-Lambert-law-based model to the in situ optical reflectometry data. To do so, the backside of the utilized glass substrate was covered with silver enabling detection of the reflected light above the sample. Assuming total reflection at the silver layer, an absorption model was used to fit the absorption edge with the concentration of chlorine as a free fit parameter. A delay in the formation of the $MAPbI_{3-x}Cl_x$ from the precursor phases was observed (**Figure 12**a-b). At an annealing temperature of 100°C, the formation of the $MAPbI_{3-x}Cl_x$ phase occurred after a delay of 35 min by incorporating the chlorine into the perovskite phase (see **Figure 12**b). In situ PL measurements were performed simultaneously to monitor the evolution of the bandgap energy and PL intensity of the thin film during annealing. The in situ PL measurements supported the hypothesis of delayed chlorine incorporation revealing that the $MAPbI_{3-x}Cl_x$-formation follows a complex transformation mechanism (**Figure 12**a). The delay in the incorporation of chlorine into $MAPbI_3$ was attributed to the presence of excess chlorine in the drying film, similarly to the case of the latent stage discussed in section 9.1.4.3. The incorporation of the chlorine into the perovskite phase occurs upon the evaporation of sufficient amount of the excess chlorine and decomposition of the Cl-containing crystalline precursor phase (MA_2PbI_3Cl) (**Figure 12**c-d). Furthermore, the absolute PL intensity was used to calculate the quasi-Fermi level (qFL) splitting versus annealing time following the procedure described in Ref.[46] The qFL is a measure for an upper limit of the open-circuit voltage of the corresponding solar cell. A maximum of the qFL splitting was observed indicating an optimal annealing duration for this material and demonstrate how – via multimodal characterization – this optimum can be correlated with a certain amount of chlorine-containing phase and overall chlorine content in the thin film. Correlating these two in situ measurements enabled

understanding how the chlorine content of the films influences their fundamental optical and optoelectronic properties. Employing the multimodal approach on different annealing temperatures enabled isolating the kinetic parameters of the $MAPbI_{3-x}Cl_x$ formation reaction. The multimodal measurements revealed that the films at the beginning of the annealing process contains MACl, MA_2PbI_3Cl, and $MAPbI_{3-x}Cl_x$ (with very small x), while MACl evaporates during annealing with an activation energy of ~ 84 kJ mol^{-1} before MA_2PbI_3Cl starts decomposing and feeding some of the remaining chlorine into the $MAPbI_{3-x}Cl_x$-phase with an activation energy of ~ 94 kJ mol^{-1}.

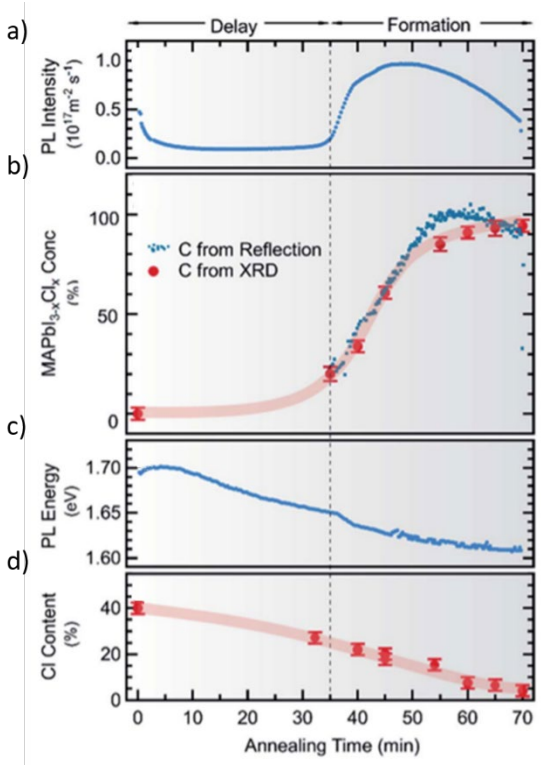

Figure 12 Time-evolution of $MAPbI_{3-x}Cl_x$ based halide perovskite properties measured by in situ PL and reflection spectroscopy as well as ex situ XRD and X-ray fluorescence spectroscopy. (a) PL intensity. (b) Different concentration of $MAPbI_{3-x}Cl_x$ thin film calculated by fitting the absorption edge of the individual reflection spectra. (c) PL peak energy (d) Decrement in Cl content in perovskite thin film as measured by XRF. Adapted with permission from Ref.[45]

Combined in situ PL and synchrotron-based GIWAXS measurements were used to reveal the thin-film formation of $MAPbI_3$ during the spin coating and subsequent annealing.[48] **Figure 13** shows the experimental setup which can be attached to a synchrotron diffraction end station

and was used for the multimodal characterization of $MAPbI_3$ formation. The complementary insights of this multimodal approach can most clearly be described at the characterization of two crucial points during the synthesis: the antisolvent-dropping during spin coating and when reaching the final annealing temperature of 100°C (see **Figure 14**a-b). The GIWAXS data revealed that the investigated material undergoes several stages of transformations during spin-coating and subsequent annealing (**Figure 14**). During spin-coating (Stages I and II in **Figure 14**a), the film evolves from a dispersion of the solvent-precursor solution state in Stage I (visible as diffuse halos in GIWAXS during the first 24 s in **Figure 14**c) to MAPI-DMSO intermediate complexes induced by antisolvent dripping at t = 25 s. During annealing (Stages III and IV in **Figure 14**a)), the onset of the crystallization of a perovskite thin film occurs after reaching the final annealing temperature in Stage III inducing perovskite phase formation at the expense of MAPI-DMSO intermediate complexes before crystallization reaches saturation in Stage IV.

While the in situ GIWAXS results can already be used to rationalize a growth mechanism, their combination with in situ PL provides additional information. For instance, the nature of abovementioned phase transformations was identified by analyzing the PL peak position and intensity during the different growth stages (identified by GIWAXS). PL results revealed that the initial nucleation upon the antisolvent dripping exhibits a strong PL emission of about 0.1 eV blue-shifted as compared to bulk MAPI, which was attributed to an immediate growth of quantum confined MAPI nanocrystals upon antisolvent dripping (**Figure 14**b&d). The absence of MAPI diffraction peaks in GIWAXS measurements was attributed to their low volume density in the film compared to the solvent-complex phase, which likely forms the major component of the film at this stage. However, the PL signal is clearly visible because of the high sensitivity of PL to even small amounts of MAPI crystallites due to their high quantum yield. Furthermore, the shape of the corresponding PL peaks, i.e. their FWHM, provided information on the distribution of these nanocrystals upon dripping antisolvent and at later stages. Upon antisolvent dripping, blue-shifted, broad, and asymmetric PL signals were observed indicating a broad size distribution of nanocrystals. It should be noted, however, that the blue-shifted, broad, and asymmetric PL signals upon antisolvent dripping can also be interpreted as emission from a very luminescent complex composition of precursor and solvent molecules or these

constituents might form a luminescent low-dimensional cluster. A similar argument was presented in a different in situ PL study and the corresponding discussion is ongoing.[49] At later times, the size of the nanocrystals homogenizes and increases due to cluster coalescence during the rest of the spin-coating, co-existing with the non-luminescent solvent complexes. When reaching the annealing temperature, PL complements the information extracted from GIWAXS data. It shows that the transformation process from both the nanocrystals and the solvent complexes to the solvent-free perovskite thin film occurs via a re-dissolution and nucleation processes. From top to bottom of the film, the solvent is removed inducing growth of highly emissive, quantum confined MAPI-clusters, whose growth and homogenization again become visible via a shift of the PL signal and its FWHM. The observed PL signature is very similar to the first nucleation event observed upon antisolvent dropping.

This study nicely shows how multimodal characterization helps to gain a better picture of a complex and fast crystallization process. While GIWAXS was not suited in this study to detect small quantities of early nucleation species, the non-luminescent solvent-colloids appearing before the antisolvent dripping could not be detected with PL. The multimodal nature of this study provided novel clues on the dynamic interplay of phases and structures during halide perovskite synthesis. It might also indicate why reproducibility is difficult from lab to lab including the reproducibility of high-quality devices in the same lab given the fast changes of thermodynamically versus kinetically driven processes. Multimodal in situ studies can be used to rationalize synthesis parameter choice and film optimization. It should be noted that multimodal in situ studies can further benefit from the combination of ex situ or pseudo in situ measurements. For example, Suchan et al.[45] expanded their study by break-off experiments using time-resolved PL, XRD, and XRF. They, therefore, combine the multimodal in situ study with snapshots of additional information at several points in time during the growth process. However, multimodal in situ measurements are needed to make sure that the findings of such ex situ measurements actually portray the properties of the growing crystals and are not substantially impacted by breaking off the synthesis e.g. by effects induced by a premature cool-down. Furthermore, the high time-resolution of most in situ techniques allows for much better options optimizing growth procedures ultimately improving synthesis routines.

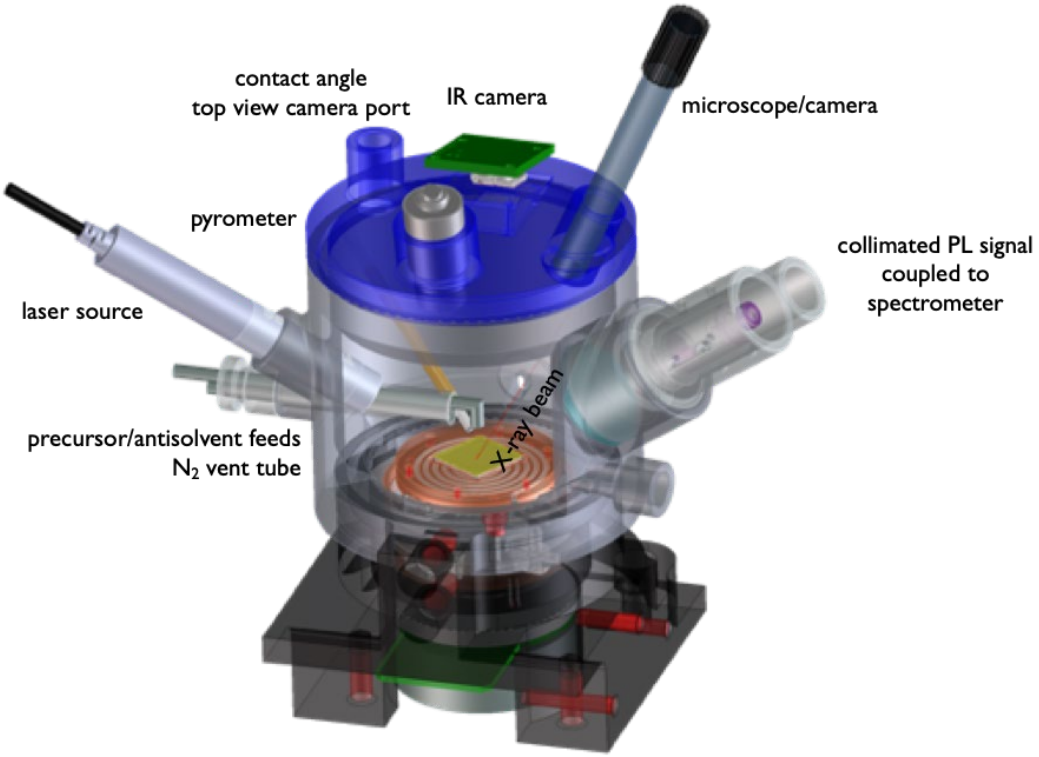

Figure 13 Schematic drawing of the experimental setup used for the multimodal study in Ref.[47] The 3D-printed housing contains an integrated spin-coater/annealing chuck as well as inlets for PL and diffraction measurements, feeds for precursors solutions and anti-solvent syringes, several optical temperature control options, as well as an N_2 flow.

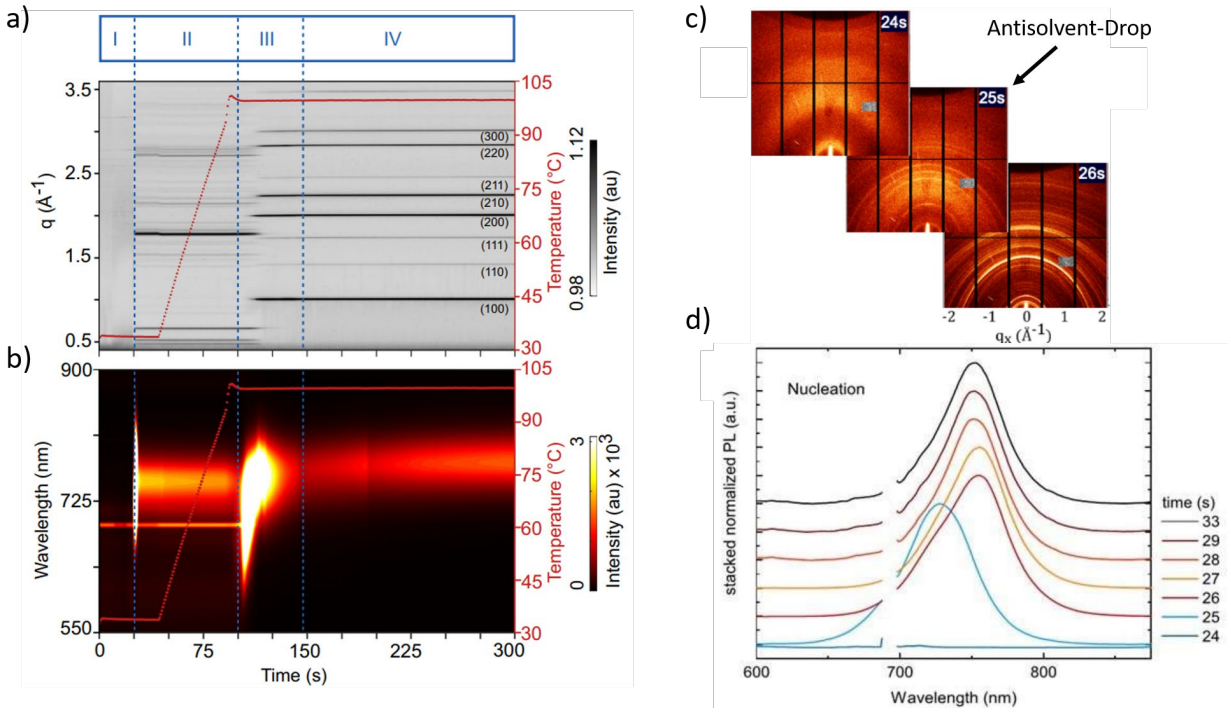

Figure 14 Multimodal view of the film evolution of MAPI using in situ GIWAXS (a) and PL (b) as well as selected GIWAXS patterns (c) and PL spectra (d). Adapted from Pratap et al.[48]

9.4 Probing Beam-Sample Interaction

At the end of this chapter, we want to turn our attention to probe beam-sample induced effects, their influence on the sample and the measurement result as well as the mitigation of beam-induced damage. Probe beam-sample interaction involves the transfer of energy (e.g. via photons) to the sample which can influence the properties of the sample and/or the kinetics of the processes under investigation for example due to local heating. The soft nature of halide perovskites and the high volatility of their constituents make them particularly susceptible to beam damage. Furthermore, in situ measurements often require rather high photon fluxes in order to achieve the desired time-resolution while maintaining a reasonable signal-to-noise ratio. Therefore, an important requirement for in situ characterization during synthesis is to find experimental conditions which allow capturing transformations at relevant time scales while minimizing the photon flux to avoid damage induced by the characterization. If the latter is not achievable due to the need for high time resolution, probe-induced modifications should

be characterized and understood. An extensive overview of possible interactions for different techniques can be found in Ref.[50]

The measurement techniques discussed above are mostly based on interactions of the evolving perovskite film with photons from monochromatic or white light, as well as X-ray sources which both can interfere with the perovskite sample during synthesis. In situ diffraction measurements are mostly performed at synchrotron sources to allow for a high time resolution. Beam damage, due to X-ray exposure, can be manifested in reduced diffraction peak intensity as well as peak shifts and can lead to radiation-induced structural changes.[50] In addition, synchrotron X-ray sources as compared to lab sources often allow for tunable X-ray photon energies which can also influence the amount of energy deposited in the material. For example, excitation above the absorption edge of lead (about 13.03 keV) will be much more efficiently absorbed by MAPI than excitation below that energy, therefore, inducing more beam damage.[50]

In the case of optical measurements, the interaction with photons from the visible spectrum can have several effects on the properties of the sample under investigation depending on the excitation power, excitation wavelength, sample properties, and measurement atmosphere.[9,51] In mixed-halide perovskites, for example, illumination with visible light can lead to an elemental redistribution, most widely known is the light-induced halide segregation,[32] which can lead to both an increase and a decrease of the PL signal depending on the energy of the used photons.[52] Furthermore, the light dose during a measurement can reduce the trap density of the perovskite.[9,53] In both cases, the measurement atmosphere plays an important role as well. The presence of oxygen and humidity can influence trap formation and passivation[54,55] and also contribute to increased and decreased PL signals.[56]

PL measurements, in general, are further influenced by charge carrier funneling (typical timescale < 1 ns)[57] towards highly emissive low bandgap regions and regions with low electronic disorder.[58] Therefore, analyzing the PL response (peak position, intensity, and FWHM) but also other optical measurement results require careful consideration of these

effects and ideally complementary measurements to probe the co-existence of compositional or structural fluctuations which might be obscured by carrier funneling.

Additionally, in situ measurements that are taken during film formation can influence the kinetics of the process under investigation. For example, it was shown that the excitation density can alter the timescale of nucleation processes in perovskites by up to two orders of magnitude.[37] However, in that study it was also found that samples across various conditions were similarly affected without altering the overall trend between samples. Therefore, this is a good example of how one can draw meaningful results despite beam-sample interaction by carefully characterizing its effect. Further possible mitigation strategies include e.g. a reduction of the exposure times by chopping the incident light. Beyond shortened exposure times, the sample spot can be moved during in situ characterization to limit beam interaction. This will, however, lead to an averaging of the property under study over a certain area and additionally exclude the possibility to laterally resolve the evolution of possibly heterogeneous functional properties.

In summary, there are manyfold experimental parameters that are crucial to monitor and be aware of in a successful and reproducible in situ measurement including preparation procedures before the actual measurements such as environment (air, N_2, vacuum), sample handling, and glove box history as well as a wide range of properties of the utilized light, and the actual measurement setup. Additionally, there is an interplay of these parameters, i.e. between the properties of the light source and the film properties as well as an amplification of beam-sample interaction in air compared to other environments.[50,52]

9.5 Summary and Outlook

Better understanding of synthesis via in situ (multimodal) characterization of different synthesis steps is powerful to gain mechanistic insights in how functional properties evolve and how they correlate to synthetic parameters and solution engineering approaches. In addition to guiding the decision on synthetic parameters to improve material performance or stability, real time characterization can also be integrated into computational machine-learning efforts to

autonomously stir experiments as well as synthesis prediction and validation of theoretical frameworks. Advancing the autonomous synthesis of perovskite materials via the development of robots and automated synthesis platforms integrated with in situ characterization techniques can pave the way to accelerate the synthesis process optimization.

The great advantage of high temporal resolution during synthesis comes at the cost of poor or no lateral resolution. This means, in order to get reasonable signal to noise data at short acquisition times large areas are measured or, in the case of spin coating a moving substrate is characterized by averaging over an area. Therefore, to truly understand synthesis both is needed, in situ characterization of synthesis followed by in depth post (ex situ) characterization of samples at very high spatial resolution. Furthermore, one critical concern is the potential beam damage of the probed materials due to exposure to high-energy X-rays or lasers depending on exposure time, flux, and the energy of the probing beam. Thus, it is of crucial importance to choose the parameters of the probing beam such that the in situ measurements don't significantly interfere with the measurement variable. Since some beam damage is imminent, care must be taken while analyzing the data to decouple the beam-related changes from the actual evolution of the measurement variable. Studies on the beam effects on the measurement variable are lacking requiring more investigations.

9.6 Acknowledgements

This work was funded by the U.S. Department of Energy (DOE), Office of Science, Office of Basic Energy Sciences, Materials Sciences and Engineering Division under Contract No. DE-AC02-05-CH11231 (D2S2 program KCD2S2). Support from the Molecular Foundry supported by the Office of Science, Office of Basic Energy Sciences, the U.S. DOE under Contract No. DE-AC02-05CH11231 is kindly acknowledged.

9.7 References

1. Kim, J. Y., Lee, J.-W., Jung, H. S., Shin, H. & Park, N.-G. High-Efficiency Perovskite Solar Cells. *Chem. Rev.* **120**, 7867–7918 (2020).
2. Saparov, B. & Mitzi, D. B. Organic–Inorganic Perovskites: Structural Versatility for Functional Materials Design. *Chem. Rev.* **116**, 4558–4596 (2016).

3. Sutter-Fella, C. M. The Value of Watching How Materials Grow: A Multimodal Case Study on Halide Perovskites. *Adv. Energy Mater.* **11**, 2003534 (2021).
4. Qin, M. *et al.* Precise Control of Perovskite Crystallization Kinetics via Sequential A-Site Doping. *Adv. Mater.* **32**, 2004630 (2020).
5. Hu, H. *et al.* Room-Temperature Meniscus Coating of >20% Perovskite Solar Cells: A Film Formation Mechanism Investigation. *Adv. Funct. Mater.* **29**, 1900092 (2019).
6. Stone, K. H. *et al.* Transformation from crystalline precursor to perovskite in PbCl2-derived MAPbI3. *Nat. Commun.* **9**, 3458 (2018).
7. Abdelsamie, M. *et al.* Impact of Processing on Structural and Compositional Evolution in Mixed Metal Halide Perovskites during Film Formation. *Adv. Funct. Mater.* **30**, 2001752 (2020).
8. Mrkyvkova, N. *et al.* Combined in Situ Photoluminescence and X-ray Scattering Reveals Defect Formation in Lead-Halide Perovskite Films. *J. Phys. Chem. Lett.* **12**, 10156–10162 (2021).
9. Babbe, F. & Sutter-Fella, C. M. Optical absorption-based in situ characterization of halide perovskites. *Adv. Energy Mater.* **10**, 1903587 (2020).
10. Sutanto, A. A. *et al.* In Situ Analysis Reveals the Role of 2D Perovskite in Preventing Thermal-Induced Degradation in 2D/3D Perovskite Interfaces. *Nano Lett.* **20**, 3992–3998 (2020).
11. Mundt, L. E. & Schelhas, L. T. Structural Evolution During Perovskite Crystal Formation and Degradation: In Situ and Operando X-Ray Diffraction Studies. *Adv. Energy Mater.* **10**, 1903074 (2020).
12. Rivnay, J., Mannsfeld, S. C. B., Miller, C. E., Salleo, A. & Toney, M. F. Quantitative Determination of Organic Semiconductor Microstructure from the Molecular to Device Scale. *Chem. Rev.* **112**, 5488–5519 (2012).
13. Hexemer, A. & Müller-Buschbaum, P. Advanced grazing-incidence techniques for modern soft-matter materials analysis. *IUCrJ* **2**, 106–125 (2015).
14. Als-Nielsen, J. (Jens) & McMorrow, Des. *Elements of modern X-ray physics*. (Wiley, 2011).
15. Müller-Buschbaum, P. The Active Layer Morphology of Organic Solar Cells Probed with Grazing Incidence Scattering Techniques. *Adv. Mater.* **26**, 7692–7709 (2014).
16. Abdelsamie, M. & Toney, M. F. *"Chapter 12: Microstructural Characterization of Conjugated Organic Semiconductors by X-Ray Scattering", Conjugated Polymers: Properties, Processing, and Applications*. (CRC Press, 2019).
17. Hammond, C. (Christopher). *The basics of crystallography and diffraction*. (Oxford University Press, 2009).
18. Müller-Buschbaum, P. A Basic Introduction to Grazing Incidence Small-Angle X-Ray Scattering. in 61–89 (Springer, Berlin, Heidelberg, 2009). doi:10.1007/978-3-540-95968-7_3.
19. Schlipf, J. & Müller-Buschbaum, P. Structure of Organometal Halide Perovskite Films as Determined with Grazing-Incidence X-Ray Scattering Methods. *Adv. Energy Mater.* **7**, 1700131 (2017).
20. Barrows, A. T. *et al.* Monitoring the Formation of a CH3NH3PbI3–xClx Perovskite during Thermal Annealing Using X-Ray Scattering. *Adv. Funct. Mater.* **26**, 4934–4942 (2016).
21. Young, K. E., Evans, C. A., Hodges, K. V., Bleacher, J. E. & Graff, T. G. A review of the handheld X-ray fluorescence spectrometer as a tool for field geologic investigations on Earth and in planetary surface exploration. *Appl. Geochem.* **72**, 77–87 (2016).

22. Dunlap-Shohl, W. A., Zhou, Y., Padture, N. P. & Mitzi, D. B. Synthetic Approaches for Halide Perovskite Thin Films. *Chem. Rev.* **119**, 3193–3295 (2019).
23. Warren, B. E. *X-Ray Diffraction*. (Dover Publications, Inc., 1990).
24. Proppe, A. H. *et al.* Multication perovskite 2D/3D interfaces form via progressive dimensional reduction. *Nat. Commun.* **12**, 3472 (2021).
25. Herz, L. M. Charge-Carrier Dynamics in Organic-Inorganic Metal Halide Perovskites. *Annu. Rev. Phys. Chem.* **67**, 65–89 (2016).
26. Baranowski, M. & Plochocka, P. Excitons in metal-halide perovskites. *Adv. Energy Mater.* **10**, 1903659 (2020).
27. Tian, Y. *et al.* Mechanistic insights into perovskite photoluminescence enhancement: light curing with oxygen can boost yield thousandfold. *Phys. Chem. Chem. Phys.* **17**, 24978–24987 (2015).
28. Milot, R. L., Eperon, G. E., Snaith, H. J., Johnston, M. B. & Herz, L. M. Temperature-dependent charge-carrier dynamics in CH3NH3PbI3 perovskite thin films. *Adv. Funct. Mater.* **25**, 6218–6227 (2015).
29. De Wolf, S. *et al.* Organometallic halide perovskites: sharp optical absorption edge and its relation to photovoltaic performance. *J. Phys. Chem. Lett.* **5**, 1035–1039 (2014).
30. Even, J., Pedesseau, L., Dupertuis, M.-A., Jancu, J.-M. & Katan, C. Electronic model for self-assembled hybrid organic/perovskite semiconductors: Reverse band edge electronic states ordering and spin-orbit coupling. *Phys. Rev. B* **86**, 205301 (2012).
31. Gfroerer, T. H. Photoluminescence in Analysis of Surfaces and Interfaces. in *Encyclopedia of Analytical Chemistry* (John Wiley & Sons, Ltd, 2006). doi:10.1002/9780470027318.a2510.
32. Liu, M. *et al.* Suppression of temperature quenching in perovskite nanocrystals for efficient and thermally stable light-emitting diodes. *Nat. Photonics* **15**, 379–385 (2021).
33. McClelland, A. & Mankin, M. *Optical measurements for scientists and engineers: a practical guide*. (Cambridge University Press, 2018).
34. Rappich, J., Kaspari, C., Camus, C. & Nickel, N. H. Fast Optical Reflectance Measurements during Spin Coating and Annealing of Organic–Inorganic Perovskite Precursor Solutions. *Phys. Status Solidi B* **258**, 2000479 (2021).
35. Ghosh, T. *et al.* Optical and structural properties of lead iodide thin films prepared by vacuum evaporation method. *Cryst. Res. Technol. J. Exp. Ind. Crystallogr.* **43**, 959–963 (2008).
36. Li, X. *et al.* A vacuum flash–assisted solution process for high-efficiency large-area perovskite solar cells. *Science* (2016) doi:10.1126/science.aaf8060.
37. Song, T.-B. *et al.* Revealing the dynamics of hybrid metal halide perovskite formation via multimodal in situ probes. *Adv. Funct. Mater.* **30**, 1908337 (2020).
38. Wagner, L. *et al.* Distinguishing crystallization stages and their influence on quantum efficiency during perovskite solar cell formation in real-time. *Sci. Rep.* **7**, 1–6 (2017).
39. Hsieh, T.-Y., Huang, C.-K., Su, T.-S., Hong, C.-Y. & Wei, T.-C. Crystal growth and dissolution of methylammonium lead iodide perovskite in sequential deposition: correlation between morphology evolution and photovoltaic performance. *ACS Appl. Mater. Interfaces* **9**, 8623–8633 (2017).
40. Nie, W. *et al.* High-efficiency solution-processed perovskite solar cells with millimeter-scale grains. *Science* **347**, 522–525 (2015).

41. Akkerman, Q. A. *et al.* Solution synthesis approach to colloidal cesium lead halide perovskite nanoplatelets with monolayer-level thickness control. *J. Am. Chem. Soc.* **138**, 1010–1016 (2016).
42. Do, M. *et al.* Low-dimensional perovskite nanoplatelet synthesis using in situ photophysical monitoring to establish controlled growth. *Nanoscale* **11**, 17262–17269 (2019).
43. Zhang, W. *et al.* Ultrasmooth organic–inorganic perovskite thin-film formation and crystallization for efficient planar heterojunction solar cells. *Nat. Commun.* **6**, 1–10 (2015).
44. van Franeker, J. J. *et al.* Monitoring thermal annealing of perovskite solar cells with in situ photoluminescence. *Adv. Energy Mater.* **7**, 1601822 (2017).
45. Suchan, K., Just, J., Becker, P., Unger, E. L. & Unold, T. Optical in situ monitoring during the synthesis of halide perovskite solar cells reveals formation kinetics and evolution of optoelectronic properties. *J. Mater. Chem. A* **8**, 10439–10449 (2020).
46. Ross, R. T. Some thermodynamics of photochemical systems. *J. Chem. Phys.* **46**, 4590–4593 (1967).
47. Pratap, S. *et al.* Probing the in-situ dynamics of structure-property evolution in hybrid perovskite thin films spincoated from complex fluids by a custom designed, beamline compatible multimodal measurement chamber. *Acta Crystallogr Sect Found Adv* **75**, A155–A156 (2019).
48. Pratap, S. *et al.* Out-of-equilibrium processes in crystallization of organic-inorganic perovskites during spin coating. *Nat. Commun.* **12**, 1–9 (2021).
49. Li, J., Dobrovolsky, A., Merdasa, A., Unger, E. L. & Scheblykin, I. G. Luminescent intermediates and humidity-dependent room-temperature conversion of the MAPbI3 perovskite precursor. *ACS Omega* **3**, 14494–14502 (2018).
50. Hoye, R. L. *et al.* Perovskite-inspired photovoltaic materials: Toward best practices in materials characterization and calculations. *Chem. Mater.* **29**, 1964–1988 (2017).
51. Quitsch, W.-A. *et al.* The role of excitation energy in photobrightening and photodegradation of halide perovskite thin films. *J. Phys. Chem. Lett.* **9**, 2062–2069 (2018).
52. Goetz, K. P., Taylor, A. D., Paulus, F. & Vaynzof, Y. Shining light on the photoluminescence properties of metal halide perovskites. *Adv. Funct. Mater.* **30**, 1910004 (2020).
53. DeQuilettes, D. W. *et al.* Photo-induced halide redistribution in organic–inorganic perovskite films. *Nat. Commun.* **7**, 1–9 (2016).
54. Knight, A. J. *et al.* Electronic traps and phase segregation in lead mixed-halide perovskite. *ACS Energy Lett.* **4**, 75–84 (2018).
55. Chen, S. *et al.* Light illumination induced photoluminescence enhancement and quenching in lead halide perovskite. *Sol. Rrl* **1**, 1600001 (2017).
56. Brenes, R. *et al.* Metal halide perovskite polycrystalline films exhibiting properties of single crystals. *Joule* **1**, 155–167 (2017).
57. Yuan, M. *et al.* Perovskite energy funnels for efficient light-emitting diodes. *Nat. Nanotechnol.* **11**, 872–877 (2016).
58. Frohna, K. *et al.* Nanoscale chemical heterogeneity dominates the optoelectronic response of alloyed perovskite solar cells. *Nat. Nanotechnol.* 1–7 (2021).